Research Article | Open Access

Microstructures

Dong et al. Microstructures 2026, 6, 2026092 DOI:10.20517/microstructures.2026.07

Synergistic regulation of barocaloric and magnetocaloric effects in Ni_2MnGa: a quantitative phase field study

Min Dong[1], Jiecheng Liu[1], Haoyu Wang[1], Zheng Wang[2], Zhuhong Liu[1], Jun Chen[3], Houbing Huang[4], Xiaoming Shi[1], Xingqiao Ma[1]

Keywords:
Ni_2MnGa, phase-field simulation, martensitic transformation, barocaloric effect, magnetocaloric effect, multicaloric effect

Citation: Dong, M.; Liu, J.; Wang, H.; Wang, Z.; Liu, Z.; Chen, J.; Huang, H.; Shi, X.; Ma, X. Synergistic regulation of barocaloric and magnetocaloric effects in Ni_2MnGa: a quantitative phase field study. *Microstructures* **2026**, *6*, 2026092. https://dx.doi.org/10.20517/microstructures.2026.07

Received: 10 Jan 2026 **First Decision:** 18 Mar 2026 **Revised:** 18 May 2026 **Accepted:** 21 May 2026 **Published:** 8 Jul 2026

Academic Editor: Zaiping Guo **Copy Editor:** Ting-Ting Hu **Production Editor:** Ting-Ting Hu

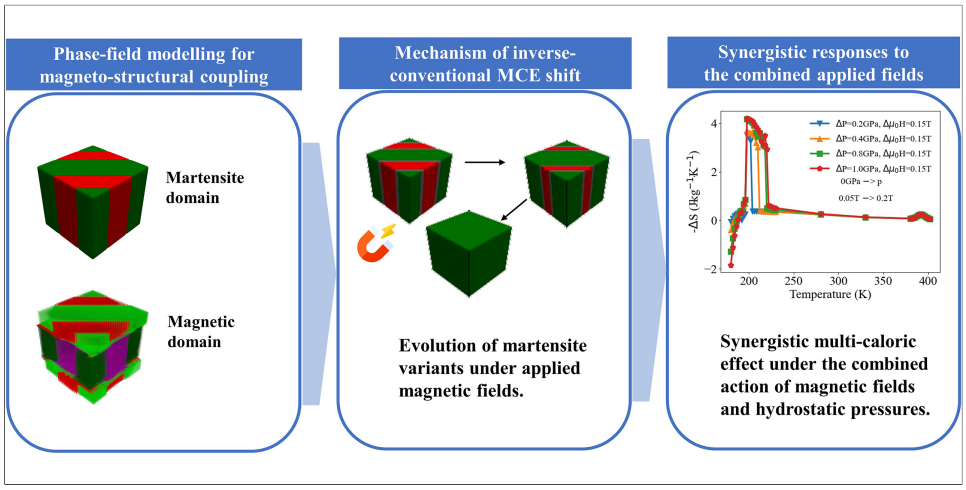

Abstract

The central challenge in achieving efficient solid-state refrigeration is the harnessing of the synergistic interplay between barocaloric and magnetocaloric effects. In this study, a quantitative phase-field model is developed to elucidate the cooperative enhancement mechanism of multicaloric effects under coupled fields in the ferromagnetic shape-memory alloy Ni_2MnGa. As demonstrated by simulations, the application of hydrostatic pressure results in a linear increase in the martensitic transformation temperature by approximately 24 K/GPa. Concurrently, this pressure-induced process generates a substantial barocaloric response. In the context of the magnetocaloric effect, an anomalous non-monotonic behaviour emerges in proximity to the phase transition. The application of weak magnetic fields results in an inverse magnetocaloric effect, characterised by a positive magnetocaloric coefficient ($\Delta S > 0$), while strong fields reverse this effect, resulting in a negative magnetocaloric coefficient ($\Delta S < 0$). Microstructural analysis corroborates the

[1]Department of Physics, University of Science and Technology Beijing, Beijing 100083, China.
[2]School of Science, Guilin University of Aerospace Technology, Guilin 541004, Guangxi, China.
[3]Beijing Advanced Innovation Center for Materials Genome Engineering, Department of Physical Chemistry, University of Science and Technology Beijing, Beijing 100083, China.
[4]School of Interdisciplinary Science, Beijing Institute of Technology, Beijing 100081, China.

Correspondence to: Dr. Xiaoming Shi, Prof. Xingqiao Ma, Department of Physics, University of Science and Technology Beijing, Beijing 100083, China. E-mail: xmshi@ustb.edu.cn; xqma@sas.ustb.edu.cn

underlying cause of this effect as being attributed to magneto-structural entropy changes. It is imperative to note that hydrostatic pressure exerts a significant suppression effect on this anomalous magnetocaloric response. Furthermore, the synergistic application of 1GPa pressure and a 0.75 T magnetic field yields an entropy change |ΔS| of 4.46 $J \cdot kg^{-1} \cdot K^{-1}$, which exceeds the sum of the individual field effects, thereby demonstrating positive magnetoelastic coupling for synergistic enhancement. The present study offers significant theoretical and simulation-based insights into the design of high-performance multicaloric cooling materials.

INTRODUCTION

Confronted with mounting environmental challenges, researchers across disciplines are dedicated to developing innovative technologies. In the refrigeration field, solid-state refrigeration has emerged as an environmentally friendly technology with enormous application potential, serving as a promising alternative to the currently dominant vapor compression refrigeration (VCR) technology. In fact, solid-state refrigeration has gradually garnered significant attention from the research community and industry. Solid-state refrigeration is fundamentally based on the caloric effect, which encompasses four categories: magnetocaloric effect (MCE), electrocaloric effect (ECE), elastocaloric effect (eCE), and barocaloric effect (BCE)[1]. These effects correspond to the thermal responses of ferroic materials under magnetic, electric, uniaxial stress, and hydrostatic pressure fields, respectively.

Over the past few decades, MCE and ECE have been intensively studied by researchers worldwide, resulting in numerous academic papers and experimental-stage devices[2,3]. In the last two decades, research focus has gradually shifted toward eCE, which can be further divided into the eCE (strictly defined as thermal response under cyclic uniaxial stress)[4] and the BCE (thermal response under cyclic hydrostatic pressure)[5]. Specifically, for BCE, an increase in external hydrostatic pressure typically leads to a rise in the barocaloric system's temperature, while a decrease in external pressure results in a corresponding drop in temperature[6]. Compared with other solid-state refrigeration technologies, barocaloric refrigeration offers distinct advantages: it provides high cooling capacity and a simple structure, avoiding the drawbacks of MCE (requiring large magnets) and ECE (risk of electrical breakdown)[7].

Since Stern-Taulats[1] *et al.* and Kitanovski *et al.*[3] published pioneering studies providing solid experimental evidence for BCE, research on barocaloric materials has boomed[8,9]. Most reported BCEs originate from first-order or second-order structural phase transitions, observed in materials such as shape memory alloys (SMAs)[10], ferroelastic fluorides[11], ferroelectrics[12], and plastic crystals[13]. Notably, some materials exhibit BCE without undergoing phase transitions, including lithium nitride (LiN)[14], polydimethylsiloxane (PDMS) rubber[15], and vulcanized natural rubber[16].

Among various barocaloric materials, SMAs have attracted considerable attention due to their unique physical properties. In particular, ferromagnetic shape memory alloys (FSMAs) - a special subclass of SMAs - possess both structural and magnetic order, enabling them to undergo magnetostructural phase transitions under external stimuli such as temperature, magnetic field, and stress field[17]. During stress- or magnetic field-induced martensitic transformation and reverse transformation, FSMAs release or absorb a large amount of latent heat, thereby exhibiting significant caloric effects[18]. This implies that FSMAs can generate both mechanical caloric effects and MCE, even simultaneously. Consequently, FSMAs are classified as multiferroic materials (exhibiting two or more ferroic orders), and the coupling between ferroic orders gives rise to the multicaloric effect - where multiferroic materials respond to multiple external stimuli with entropy and temperature change[19]. SMAs are capable of producing enormous eCE; for example, Ni-Mn-Ti alloys exhibit an adiabatic temperature change (ΔT) of up to 31.5 K[20], and Ni-Fe-Ga alloys show a ΔT of 13.5 K[21]. Additionally, the magnetoelastic coupling in FSMAs can potentially enhance the caloric effect and enable the regulation of refrigeration processes[22].

Based on the above research background, this work selects Ni_2MnGa - a typical FSMA - as the research object to investigate its performance under combined magnetic field and hydrostatic pressure. Although Ni_2MnGa exhibits inherent brittleness, theoretical exploration and simulation of this alloy remain of great significance for elucidating its functional mechanisms and providing insights into other FSMA systems[23]. Currently, numerous experimental[24] and simulation[25] studies on Ni_2MnGa have been reported. Researchers such as Wu *et al*. and Ohmer *et al*. have simulated the magnetostructural properties of Ni_2MnGa using phase-field modeling, and several computational models based on different methods have been developed[26,27]. Compared with other simulation methods, phase-field modeling is particularly effective in investigating the evolution of microstructures (i.e., magnetic domains and martensitic variants) and in capturing the evolution of physical properties under different external fields, thus providing detailed insights into evolutionary processes[28]. However, the majority of the aforementioned studies grounded in micromagnetism employ the Landau-Lifshitz-Gilbert (LLG) equation, which only evolves the magnetization and is independent of temperature. This results in inaccurate calculations of thermal effects[29].

To address this limitation, this work develops a phase-field model incorporating two time-dependent Ginzburg-Landau (TDGL) equations to compute the magnetic moment and the martensitic variant transformation fraction, respectively. The TDGL equation is a theoretical framework that evolves the phase-field variables of a system via the free energy, which is inherently temperature-dependent and a function of multiple characteristic variables of the system. This makes it a more suitable tool for discussing phase transitions and multi-physics field problems. This model simulates the evolution of martensitic variants and magnetic domains in Ni_2MnGa under combined external hydrostatic pressure and a magnetic field. Subsequently, the isothermal entropy change (ΔS) and adiabatic temperature change (ΔT) are calculated based on the Maxwell relations. As a FSMA, Ni_2MnGa exhibits both magnetocaloric and BCE; therefore, this work focuses on investigating the factors influencing its BCE, with particular emphasis on the coupling between magnetocaloric and BCE.

The remainder of this paper is organized as follows: The section entitled “Materials and Methods” provides a comprehensive overview of the phase-field model of Ni_2MnGa and the calculation of caloric effects via Maxwell relations. The section entitled “Results and Discussion” provides a detailed exposition of the simulation of the fundamental physical properties of Ni_2MnGa, as well as BCE, MCE and the multicaloric effect.

MATERIALS AND METHODS

The present study aims to systematically investigate the BCE of Ni_2MnGa FSMA and to clarify the regulatory role of external magnetic fields. To this end, a comprehensive theoretical framework has been established. The research process is predicated on a two-step core logic. Firstly, phase-field simulation was employed to capture the magnetostructural phase transition (MSPT) behavior of Ni_2MnGa under combined hydrostatic pressure and magnetic field. Secondly, Maxwell relations were applied to quantify the key caloric performance metrics, i.e., isothermal entropy change (ΔS) and adiabatic temperature change (ΔT). The following section details the phase-field model and the calculation methods.

Phase-field model

The phase-field simulation methodology is predicated on the principle of minimizing the total Gibbs free energy of the system. This approach is inherently capable of describing the temporal and spatial evolution of microstructures (e.g., martensitic variants and magnetic domains) during phase transitions. The total Gibbs free energy E of Ni_2MnGa comprises seven energy components, namely chemical energy (f_{ch}), elastic strain

energy (f_{el}), magnetocrystalline anisotropy energy (f_{mc}), exchange energy (f_{exch}), magnetostatic energy (f_{ms}), magnetoelastic coupling energy (f_{me}), and Zeeman energy (f_{zm}). The integral form of the total free energy is expressed as[30]:

$$E = \int_V (f_{\mathrm{ch}} + f_{el} + f_{mc} + f_{exch} + f_{ms} + f_{me} + f_{zm})\, dV \tag{1}$$

where V denotes the total volume of the simulation system. The formulation of each energy component and the temporal evolution equations is derived from the intrinsic physical properties of Ni_2MnGa as detailed below:

f_{ch} is responsible for the interfacial energy between distinct phases and the bulk free energy difference between martensite and austenite. It can be expressed mathematically as follows:

$$f_{ch} = \int_V \left[\frac{1}{2}\beta \sum_{p=1}^{v} \left(\nabla \eta_p\right)^2 + f_0\left(\{\eta_p\}\right) \right] dV \tag{2}$$

where the first term of the right-hand side represents the gradient energy (β is gradient energy coefficients and ∇ is referred to as the gradient operator), and the second term $f_0(\{\eta_p\})$ represents the bulk free energy that has been expanded into a Landau polynomial:

$$f_0 = \frac{1}{2}A \sum_{p=1}^{3} \eta_p^2 - \frac{1}{3}B \sum_{p=1}^{3} \eta_p^3 + \frac{1}{4}C \left(\sum_{p=1}^{3} \eta_p^2 \right)^2 \tag{3}$$

Where $\{\eta_p(p = 1,2,3)\}$ represent structural order parameters ($\{\eta_p(p = 1,2,3) = 0\}$ for austenite, $\{\eta_p(p = 1,2,3 \neq 0)\}$ for tetragonal martensite variants). A, B and C are Landau coefficients that are expressed as $A = 32\Delta G^*$, $B = 3A\text{-}12\Delta G_m$, $C = 2A\text{-}12\Delta G_m$. $\Delta G_m = Q\,(T\text{-}T_M)/T_M$ is the driving force of martensitic transformation and Q is latent heat of martensitic transformation, T_M is martensitic transformation temperature, T is ambient temperature[31]. ΔG^* is the energy barrier based on literature[32]:

$$\Delta G^* = Q\left(7.0 + \frac{T - T_M}{T_M}\right)/32 \tag{4}$$

f_{el} originates from lattice mismatch and elastic relaxation. According to Khachaturyan (KS) microelasticity theory, this energy can be further decomposed into three distinct components: intrinsic strain energy (E_0), homogeneous relaxation energy $\left(E_{\mathrm{relax}}^{\mathrm{homo}}\right)$ and heterogeneous relaxation energy $\left(E_{\mathrm{relax}}^{\mathrm{heter}}\right)$:

$$f_{el} = E_0 + E_{\mathrm{relax}}^{\mathrm{homo}} + E_{\mathrm{relax}}^{\mathrm{heter}} \tag{5}$$

$$E_0 = \frac{V}{2} \sum_{p=1}^{3} c_{ijkl} \varepsilon_{ij}^{00}(p) \varepsilon_{kl}^{00}(p) \frac{1}{V} \int_V \eta_p(\boldsymbol{r})^2 dV \tag{6}$$

$$E_{\mathrm{relax}}^{\mathrm{homo}} = -\frac{V}{2} \sum_{p=1}^{3} \sum_{q=1}^{3} c_{ijkl} \varepsilon_{ij}^{00}(p) \varepsilon_{kl}^{00}(q) \frac{1}{V} \int_V \eta_p(\boldsymbol{r})^2 dV \frac{1}{V} \int_V \eta_q(\boldsymbol{r})^2 dV \tag{7}$$

$$E_{\mathrm{relax}}^{\mathrm{heter}} = -\frac{1}{2} \sum_{p=1}^{3} \sum_{q=1}^{3} \frac{1}{V} \int_V B_{pq} \left(\frac{\boldsymbol{k}}{k}\right)^2 \tilde{\eta}_p(\boldsymbol{k}) \tilde{\eta}_q(\boldsymbol{k}) \frac{d^3\boldsymbol{k}}{(2\pi)^3} \tag{8}$$

$$B_{pq}(\boldsymbol{e}) = e_i \varepsilon_{ij}^{00}(p) \Omega_{jk}(\boldsymbol{e}) \varepsilon_{kl}^{00}(q) e_l \tag{9}$$

The f_{el} is calculated via KS microelasticity theory. $\boldsymbol{k}$ is the reciprocal lattice vector, and $\boldsymbol{e} = /\frac{\boldsymbol{k}}{k}/$ is the unit vector along the $\boldsymbol{k}$ direction. $\tilde{\eta}_p(\boldsymbol{k})$ is the Fourier transform of $\eta_p(\boldsymbol{r})$. $\Omega_{ij}(\boldsymbol{e})$ are the Green's tensors inverse to $\Omega_{ij}(\boldsymbol{e})^{-1} = c_{ijkl} e_k e_l$. c_{ijkl}. is the elastic modulus tensor. $\varepsilon_{ij}^{00}(p)$ is the stress-free strain of pth martensite variant characterised by

$$\varepsilon^{00}(1)=\begin{pmatrix}\varepsilon_1&0&0\\0&\varepsilon_2&0\\0&0&\varepsilon_2\end{pmatrix},\varepsilon^{00}(2)=\begin{pmatrix}\varepsilon_2&0&0\\0&\varepsilon_1&0\\0&0&\varepsilon_2\end{pmatrix},\varepsilon^{00}(3)=\begin{pmatrix}\varepsilon_2&0&0\\0&\varepsilon_2&0\\0&0&\varepsilon_1\end{pmatrix}$$

where $\varepsilon_1 = (c_M\text{-}a_c)/a_c$, $\varepsilon_2 = (a_M\text{-}a_c)/a_c$. a_c is the crystal lattice parameter of the cubic austenite phase and a_M, c_M are the crystal lattice parameters of the tetragonal-like martensite phase. The magnetic energy components are comprised of four subcomponents that describe magnetic behavior:

(1) Magneto-crystalline anisotropy energy:

$$f_{mc}=\int_V\frac{1}{2}a_1\boldsymbol{m}^2+\frac{1}{4}a_{11}\boldsymbol{m}^4+a_{12}\left(m_x^2m_y^2+m_x^2m_z^2+m_y^2m_z^2\right)dV \tag{10}$$

where $\boldsymbol{m} = |\boldsymbol{M}/M_o|$ is the unit vector of the magnetisation and M_o the saturation magnetisation. a_1 and a_{11} are exchange parameters. a_{12} is the first cubic anisotropic constant.

(2) f_{exch}:

$$f_{\text{exch}}=A\int(\nabla\boldsymbol{m})^2dV \tag{11}$$

where A is an exchange stiffness constant.

(3) f_{ms}:

$$f_{ms}=-\frac{1}{2}\mu_0M_s\int H_d\cdot\boldsymbol{m}dV \tag{12}$$

where μ_0 is the vacuum permeability, and H_d is the demagnetization field arising from long-range interactions among magnetic moments.

(4) f_{me}:

$$f_{me}=\int\left[\gamma_0e_1\boldsymbol{m}^2+\gamma_1\left(\frac{1}{2}e_2\left(m_x^2-m_y^2\right)+\frac{1}{6}e_3\left(3m_z^2-\boldsymbol{m}^2\right)\right)\right]dV \tag{13}$$

where γ_0, γ_1 are the volume and anisotropic magnetostriction constants. e_i'*s* are functions of stress-free strains of martensitic variants that is expressed as[33]

$$\begin{aligned}e_1&=\frac{1}{\sqrt{3}}\sum_{i=1}^{3}\left(\sum_{p=1}^{3}\eta_p\varepsilon_{ii}^{00}(p)\right)\\e_2&=\frac{1}{\sqrt{2}}\left(\sum_{p=1}^{3}\eta_p\varepsilon_{11}^{00}(p)-\sum_{p=1}^{3}\eta_p\varepsilon_{22}^{00}(p)\right)\\e_3&=\frac{1}{\sqrt{6}}\left(2\sum_{p=1}^{3}\eta_p\varepsilon_{33}^{00}(p)-\sum_{p=1}^{3}\eta_p\varepsilon_{11}^{00}(p)-\sum_{p=1}^{3}\eta_p\varepsilon_{22}^{00}(p)\right)\end{aligned} \tag{14}$$

(5) f_{zm}:

$$f_{zm}=\int_V\boldsymbol{H}\cdot\boldsymbol{m}dV \tag{15}$$

where $\boldsymbol{H}$ is applied external magnetic fields.

Temporal evolution equations: The evolution of structural order parameters η_p and magnetic order parameters $\boldsymbol{m}$ are governed by TDGL equations for free energy minimization:

Table 1. Material and simulation parameters for Ni_2MnGa

Parameters	Values	Unit	Source
T_M	202	K	[35]
T_C	380	K	[35]
Latent heat (Q)	1.99	kJ/kg	[35]
Elastic modulus (C_{11})	1.6×10^{11}	N/m²	[26]
Elastic modulus (C_{12})	1.52×10^{11}	N/m²	[26]
Elastic modulus (C_{44})	0.43×10^{11}	N/m²	[26]
a_1	$5.39 \times 10^5 \times \left(\exp\left(\frac{T - T_C}{5\,0}\right)/T_C + 0.01\right) \times (T - T_C)$	J/m³	This work
a_{11}	13.475×10^5	J/m³	This work
a_{12}	3.138×10^5	J/m³	This work
γ_0	1.0×10^7	J/m³	This work
γ_1	0.4×10^7	J/m³	This work
M_s	88.1 (at 180 K)	A·m²/kg	[35]

T_M: Martensitic transformation temperature; T_C: curie temperature; M_s: saturation magnetization.

$$\frac{\partial \eta_p(\boldsymbol{r},t)}{\partial t} = -L_\eta \frac{\delta E}{\delta \eta_p(\boldsymbol{r},t)} \tag{16}$$

$$\frac{\partial \boldsymbol{m}(\boldsymbol{r},t)}{\partial t} = -L_m \frac{\delta E}{\delta \boldsymbol{m}(\boldsymbol{r},t)} \tag{17}$$

where L_η and L_m are the kinetic coefficients of the evolutions of the structural and magnetic parameters, respectively.

Simulation details: TDGL equations were solved via Gauss-Seidel projection method[34]. A $64\Delta x \times 64\Delta y \times 64\Delta z$ 3D domain ($\Delta x \times \Delta y \times \Delta z$: mesh size) with periodic boundary conditions (x/y/z axes) was adopted. To facilitate the calculation, we employed unified kinetic coefficients $L_\eta = L_m = 1.0$ (In this case, the time in our results is relative, while other physical properties remain unaffected). The remaining parameters, such as elastic modulus, were obtained from experiments and literature sources [Table 1].

Calculation of caloric effects via maxwell relations

The Maxwell relations are a set of equations that quantify caloric effects by linking entropy changes to material property responses (volume, magnetization) to external fields. They were applied to calculate ΔS and ΔT for BCE, MCE, and multicaloric effect (MCE-BCE coupling).

BCE: Isothermal entropy change from pressure variation ($p_0 \rightarrow p_1$) is

$$\Delta S_\eta\,(T; p_0 \rightarrow p_1) = \int_{p_0}^{p_1} \left(\frac{\partial V}{\partial T}\right)_p dp \tag{18}$$

where V stands for volume, p for the applied hydrostatic pressure, and T for temperature. Adiabatic temperature change is

$$\Delta T_\eta\,(S; p_0 \rightarrow p_1) = -\int_{p_0}^{p_1} \frac{T}{C_p}\left(\frac{\partial V}{\partial T}\right)_p dp \tag{19}$$

where C_p is isobaric heat capacity.

MCE Under magnetic field variation ($\mu_0 H_0 \rightarrow \mu_0 H_1$), The isothermal entropy change and the adiabatic temperature change in the MCE are calculated by the following equations:

$$\Delta S_m\left(T;\mu_0 H_0 \rightarrow \mu_0 H_1\right) = \mu_0 \int_{H_0}^{H_1} \left(\frac{\partial M}{\partial T}\right)_H dH \tag{20}$$

$$\Delta T_m\left(S;\mu_0 H_0 \rightarrow \mu_0 H_1\right) = -\mu_0 \int_{H_0}^{H_1} \frac{T}{C_H}\left(\frac{\partial M}{\partial T}\right)_H dH \tag{21}$$

where μ_0 is the vacuum permeability constant, M stands for magnetisation, H for the applied magnetic field, and T for temperature. C_H is the heat capacity at a constant magnetic field.

MCE-BCE Coupling: The isothermal entropy changes and the adiabatic temperature changes in the multicaloric effect are calculated by the following equations:

$$\begin{aligned}\Delta S_{\text{multi}}\left(\left(p_0,\mu_0 H_0\right) \rightarrow \left(p_1,\mu_0 H_1\right)\right) &= \int_{p_0}^{p_1}\left(\frac{\partial V}{\partial T}\right)_{p,\mu_0 H_0} dp + \mu_0 \int_{H_0}^{H_1}\left(\frac{\partial M}{\partial T}\right)_H dH \\ &= \int_{p_0}^{p_1}\left(\frac{\partial V}{\partial T}\right)_p dp + \mu_0 \int_{H_0}^{H_1}\left(\frac{\partial M}{\partial T}\right)_H dH + \mu_0 \int_{p_0}^{p_1}\int_{H_0}^{H_1}\frac{\partial \chi_{12}}{\partial T} dp dH\end{aligned} \tag{22}$$

where χ_{12} is the cross-susceptibility.

RESULTS AND DISCUSSION

In this study, the inverse magnetocaloric, barocaloric, and multicaloric effects induced by the martensitic transformation in stoichiometric Ni_2MnGa were simulated. Ni_2MnGa is a prototypical FSMA that manifests both ferroelasticity and ferromagnetism. Its physical properties are modifiable by applied loads and magnetic fields. At temperatures that exceed T_C, Ni_2MnGa exists in the paramagnetic austenite phase which possesses a cubic crystal structure. In the event that the temperature is lower than T_C but higher than T_M, a paramagnetic-ferromagnetic transition occurs, resulting in the system transforming into the ferromagnetic austenite phase. In the presence of a temperature lower than T_M, a transformation from the high-temperature phase to the low-temperature phase occurs, resulting in the ferromagnetic martensite phase with a tetragonal crystal structure[36]. In this phase the short crystal axis serves as the easy magnetization axis. The existence of three distinct types of martensite variants is well documented, each exhibiting an easily identifiable magnetization axis oriented along the X, Y, or Z direction.

Simulation of basic physical properties and model validation

In order to verify the reliability of the established phase-field model, the fundamental physical behaviors of Ni_2MnGa, including martensitic variant reorientation, magnetic domain evolution, and magnetization-temperature (M-T) characteristics, were initially simulated. These properties have been the subject of extensive research in previous works (including our own), and the consistency between the simulation results and existing knowledge can confirm the validity of the model. This provided a foundation for the subsequent study of caloric effects.

The temperature-dependent magnetization and the magnetic hysteresis loop at 190 K in Ni_2MnGa were calculated, in conjunction with the evolution of magnetic domains and martensite variants. In the absence of an external magnetic field, the system began from a random distribution of magnetic moments and martensitic nuclei. The system gradually developed a stable domain structure as it minimized free energy. As demonstrated in the subsequent microstructural evolution figures, two martensite variants, designated X (red) and Y (green), possessed magnetic moments that aligned along four distinct orientations. As illustrated in Figure 1A and B, the magnetic moments were represented by yellow (+X), orange (-X), blue (+Y), and

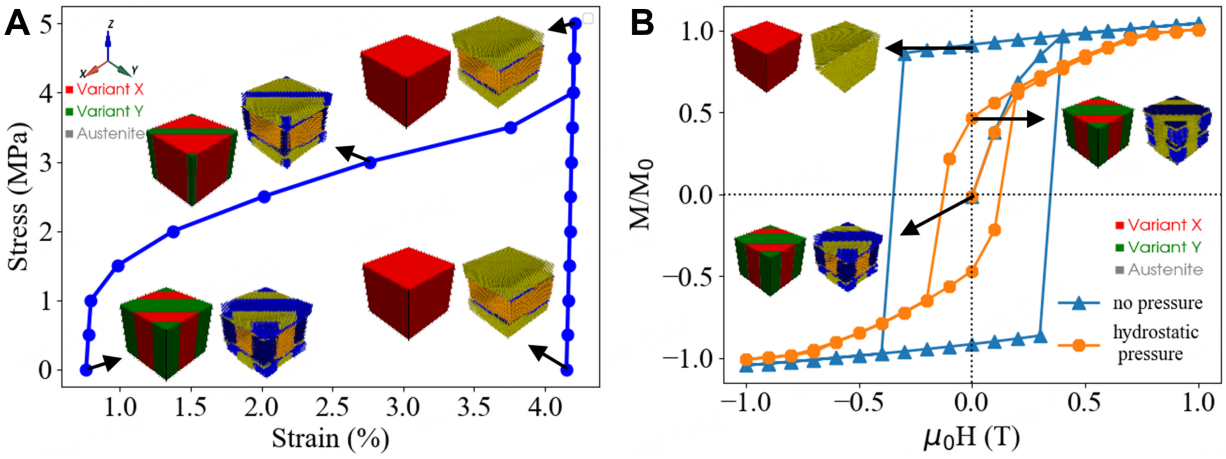

Figure 1. (A) The stress-strain curve of martensitic Ni_2MnGa at temperature of 190 K; (B) Magnetic hysteresis loops of martensitic Ni_2MnGa subject to different mechanical boundary conditions at temperature of 190 K.

dark blue (-Y). At this time, the magnetization intensity was contributed by the net magnetic moments of the two variants. Due to the symmetrical orientation of the variants, the net magnetization was very low. This domain configuration was the result of a balance between magnetocrystalline anisotropy, elastic energy, magnetoelastic coupling, and domain wall energy. Therefore, the microstructures, domains, and various properties of the Ni_2MnGa alloy were calculated under various applied magnetic fields and pressures.

Figure 1A presented the stress-strain curve of martensitic Ni_2MnGa simulated at 190 K, where a compressive stress was applied along the X-axis, increasing from 0 MPa to 5 MPa with steps of 0.5 MPa. As evidenced by the stress-strain curve and the concomitant martensite domain evolution, it was discernible that twin boundaries commence movement and martensite variants rearrange at 1.5 MPa. The observed expansion of the red domain region and contraction of the green domain region were indicative of an increase in the volume fraction of martensite variants X and a decrease in that of martensite variants Y. Upon reaching a pressure of 4 MPa, all martensite variants Y underwent a transformation into martensite variants X. Subsequent to this, even under conditions of further increasing the pressure to 5 MPa and then reducing it to 0 MPa, the martensite domains persisted in a single-domain state. This observation suggested that the application of sufficiently large compressive stress resulted in the irreversible martensitic reorientation. This outcome aligned with the established martensitic reorientation behavior of Ni_2MnGa, as documented in prior research[26].

As illustrated in Figure 1B, the magnetic hysteresis loops of Ni_2MnGa are depicted under varying mechanical boundary conditions, including free boundary and 1 GPa hydrostatic pressure, at a temperature of 190 K. The initial magnetization curve demonstrated a well-defined sequence of domain structure evolution upon the application of a magnetic field along the direction +X, with a maximum value of 1 T and a step size of 0.2 T. In the presence of low magnetic fields, the Zeeman interaction facilitated the proliferation of magnetic domains +X and the retraction of magnetic domains -X. Concurrently, magnetic moments within the martensite variants Y underwent a slight rotation toward the field direction. This stage was characterized by the motion of magnetic domain walls, with no apparent structural reorientation of martensite variants. As the field strength increased, the rotation of magnetic moments in the martensite variants Y became more pronounced. The structural lattices of the martensite variants Y were driven by strong magnetoelastic coupling, resulting in a tendency to reorient toward the direction X, accompanied by the migration of martensitic twin boundaries. It had been demonstrated that the magnetic moments on opposite sides of a twin boundary are mutually perpendicular, forming a 90° magnetic domain wall. This resulted in highly

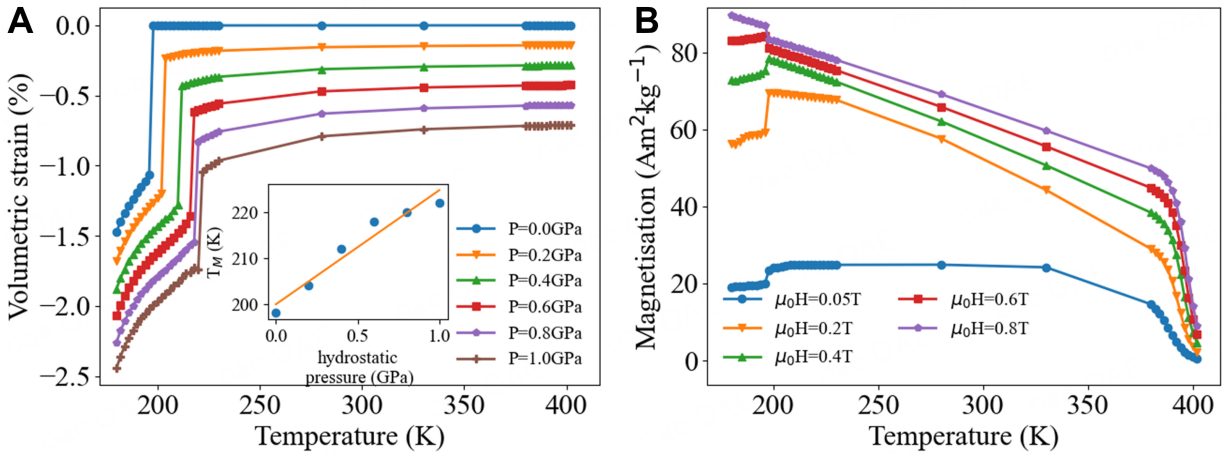

Figure 2. (A) Curves of volume strain versus temperature for Ni-Mn-Ga alloys under different hydrostatic pressures within the temperature range of 180 to 400 K. The inset shows that the martensitic transformation temperature increases with increasing applied hydrostatic pressure; (B) M (T) curves under different external magnetic fields at the range of 180 to 400 K.

synchronized motion of the 90° domain wall and twin boundary, which was a hallmark of magnetostructural coupling in Ni_2MnGa.When the applied magnetic field increased to 0.4 T, all magnetic moments aligned along the direction +X, the martensite variants Y disappeared completely, and the material fully transformed into the martensite variants X. This resulted in forming a mono-variant state. Further increasing the magnetic field, the martensite variants did not undergo any changes, but the magnetic moments rotated toward the applied field to overcome magnetocrystalline anisotropy. These magnetic moments tended to saturate at higher fields. The material's hysteresis loops were obtained by reversing the magnetic field from saturation.

Conversely, under the boundary condition of applying a hydrostatic pressure of 1 GPa, the volume fraction of martensite variants remained constant irrespective of the variation of the external magnetic field, and no magnetically induced reorientation of martensite occurs. It had been demonstrated that under the influence of hydrostatic pressure, the remanence, coercivity, and area of the magnetic hysteresis loop of the material are significantly reduced, while the saturation field was increased. This phenomenon was consistent with the regulatory effect of hydrostatic pressure on magnetic properties, as reported in the literature[26].

As illustrated in Figure 2A, the temperature-dependent volumetric strain curves of Ni_2MnGa were observed under varying hydrostatic pressures, with the temperature ranging from 180 to 400 K. The applied hydrostatic pressure was systematically varied in steps from 0 to 1 GPa, with an interval of 0.2 GPa. Each volumetric strain curve displayed an abrupt mutation at a particular temperature, a hallmark of first-order phase transitions, signifying a martensitic transformation in the material. As hydrostatic pressure increases, the entire curve shifted to higher temperatures, indicating that the martensitic transformation temperature rises accordingly. As illustrated in Figure 2A, the inset displayed the linear regression relationship between the martensitic transformation temperature and hydrostatic pressures. This relationship demonstrated a monotonically increasing trend of the phase transformation temperature with increasing hydrostatic pressure, with a slope of $dT/dP \approx 24$ K/GPa. This finding was basically consistent with the experimental data reported in reference[37].

As illustrated in Figure 2B, the simulated M-T curves of Ni_2MnGa were depicted under varying external magnetic fields, with temperatures ranging from 180 to 400 K and magnetic fields increasing from 0.05 to 0.8 T. Figure 2B demonstrated that the Curie temperature (T_C) of Ni_2MnGa was 380 K, and the martensitic

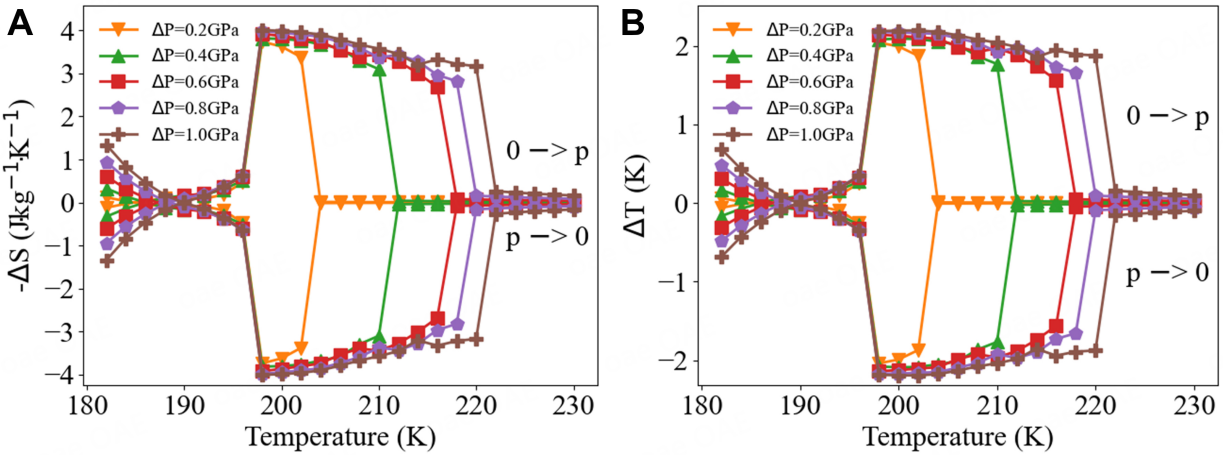

Figure 3. (A) Isothermal entropy changes of the barocaloric effect under different hydrostatic pressures; (B) adiabatic temperature changes of the barocaloric effect under different hydrostatic pressures.

transformation temperature (T_M) was 196 K. It was noteworthy that the curves in this study were cooling curves, and the inverse martensitic transformation temperature (T_A), corresponding to the heating curve, was slightly higher than T_M. At temperatures higher than T_C, the material was in the paramagnetic austenite phase. At temperatures lower than T_C but higher than T_M, it was in the ferromagnetic austenite phase. At temperatures lower than T_M, the system transformed into the ferromagnetic martensite phase, with an abrupt change in saturation magnetization at T_M. It was evident that under conditions of low magnetic field intensity, the magnetization intensity within the martensitic region was markedly lower in comparison to that of the austenitic region. However, as the magnetic field strength increased, the magnetization intensity of martensite exhibited a faster increase than that of austenite. When the external magnetic field exceeded 0.8 T, the magnetization intensity of martensite even surpassed that of austenite. This phenomenon could be attributed to the coexistence of multiple variants in martensite phase, the necessity for these variants to vary for magnetization to approach saturation, and the observation that intrinsic magnetization of the martensite phase is slightly greater than that of the austenite phase.

The simulation results for martensitic transformation reorientation, magnetic hysteresis, and M-T exhibited a high degree of consistency with existing experimental data. This finding served to fully verify the reliability of the phase-field model and to ensure the validity of subsequent caloric effect calculations.

BCE regulation by hydrostatic pressures

The isothermal entropy change (|ΔS|) and adiabatic temperature change (|ΔT|) of BCE in Ni_2MnGa were calculated using the Maxwell relation method, as depicted in Figure 2A. The volumetric strain data from Figure 2A were utilized to determine the isothermal entropy change and adiabatic temperature change of BCE in Ni_2MnGa. The calculation results were illustrated in Figure 3A and B.

In the isothermal pressurization process, characterized by an increase in hydrostatic pressure increased from 0 to p, the isothermal entropy change was represented by $\Delta S < 0$, while the adiabatic temperature change was expressed as $\Delta T > 0$. These phenomena signify a decline in entropy of the system and an increase in temperature. In the process of isothermal depressurization process, the decrease in hydrostatic pressure from p to 0 was accompanied by a positive increase in entropy ($\Delta S > 0$) and a negative decrease in temperature ($\Delta T < 0$). These characteristics confirmed the occurrence of the conventional BCE in Ni_2MnGa. The following section would examine the evolution characteristics of the BCE with temperature and pressure. (1) Shift of initial transformation temperature: as illustrated in Figure 2A, the initial martensitic transition temperature underwent a substantial shift toward higher temperatures within an increase in hydrostatic pressure. For instance, the initial phase transition temperature was estimated to be approximately 196 K at

0 GPa of pressure, increasing to approximately 220 K at 1 GPa of pressure, with a total shift of around 24 K. This is consistent with the slope dT/dP ≈ 24 K/GPa, as depicted in the inset. The underlying reason for this phenomenon is the direct correlation between the martensitic transformation temperature and the applied pressure. The unit cell volume of martensite (196.1Å^3) is smaller than that of austenite (197.3Å^3) at elevated pressures, causing the martensitic transformation temperature to increase. In circumstances involving elevated pressure, the free energy of austenite exhibits a more substantial increase, thereby enhancing the stability of martensite and concomitantly effecting an upward shift in the transformation temperature; (2) The difference between the maximum values of ΔS and ΔT was as follows: The maximum values of isothermal entropy change and adiabatic temperature change exhibited a monotonically increasing trend with the rise of hydrostatic pressure. At pressures below 0.1 GPa, the maximum |ΔS| was approximately 0.4 J·kg^{-1}·K^{-1} and the maximum |ΔT| is about 0.2 K. At the pressure of 1.0 GPa, the maximum |ΔS| reaches 4.01 J·kg^{-1}·K^{-1}, and the maximum |ΔT| reaches 2.19 K, with the values increased by an order of magnitude. This phenomenon can be attributed to the augmented driving force of the martensitic transformation under elevated hydrostatic pressure, which results in a substantial alteration in volume and entropy; (3) The rationale underlying the decline in values at low temperatures is as follows: In the event that the temperature is at a level significantly below the martensitic transformation temperature, the material undergoes a complete transformation into the martensite phase. The martensite phase is known for its exceptional structural stability, which renders it relatively impervious to variations in hydrostatic pressure, resulting in only a negligible change in its volume and entropy. Consequently, as the temperature deviates from T_M and shifts towards the lower temperatures, ΔS and ΔT gradually decrease. The maximum isothermal entropy change |ΔS| = 4.01 J·kg^{-1}·K^{-1} and adiabatic temperature change |ΔT| = 2.19 K. This determination was made under the condition of applying a maximum hydrostatic pressure of 1 GPa during the simulation. The magnitude is found to be considerably larger than the MCE of 1.10 J·kg^{-1}·K^{-1} under an applied magnetic field of 0.8 T. By comparison, the adiabatic temperature change of $Ni_{58.3}Mn_{17.1}Ga_{24.6}$ |ΔT| = 28 K[38] under the hydrostatic pressure Δp = 1.05 GPa. Consequently, engineers have the capability to substitute bulky magnetocaloric refrigeration equipment with more streamlined and effective mechanical refrigeration systems. Furthermore, in comparison with MCE, the application of hydrostatic pressure to modify the martensitic transformation temperature facilitates the operation of mechanical refrigeration systems within a temperature range that is expanded by tens of Kelvins.

MCE and its mechanism

To complement the analysis of the BCE, the MCE of Ni_2MnGa under applied magnetic fields (0.05-0.8 T) was investigated. As demonstrated in Figures 4A and B, the variations of the isothermal entropy change (ΔS) and adiabatic temperature change (ΔT) with temperature are illustrated. Distinct magnetization changes occur at both the T_C and the martensitic transformation temperature (T_M). These transitions resulted in significant caloric responses, indicative of phase transitions in the system. In the vicinity of the T_C, the second-order paramagnetic-ferromagnetic phase transition exhibited conventional MCE characteristics (ΔS < 0, ΔT > 0). It was noteworthy that in the vicinity of T_M (195-197 K), the entropy change and temperature change exhibited non-monotonic variations with applied magnetic fields. A weak field induced the inverse MCE (ΔS > 0, ΔT < 0), while a high magnetic field resulted in the conventional MCE (ΔS < 0, ΔT > 0). The transition between these regimes occurs at a critical field $\mu_0 H_C \approx 0.4$ T, where |ΔS| attained its maximum value of 1.10 J·kg^{-1}·K^{-1}. This observation is consistent with experimental findings reported in the literature[36]. In comparison, the isothermal entropy change of $Ni_{48.7}Mn_{27.6}Ga_{23.7}$ |ΔS| is approximately 1.3 J·kg^{-1}·K^{-1} under the influence of a magnetic field $\Delta\mu_0 H = 0.3$ T[39].

As illustrated in Figure 5A, the total, structural, and magnetic entropy changes ΔS are plotted against magnetic fields at 196 Kelvin. It is noteworthy that the minor configurational entropy change was incorporated within the structural entropy change contribution. The entropy change evolution reveals two

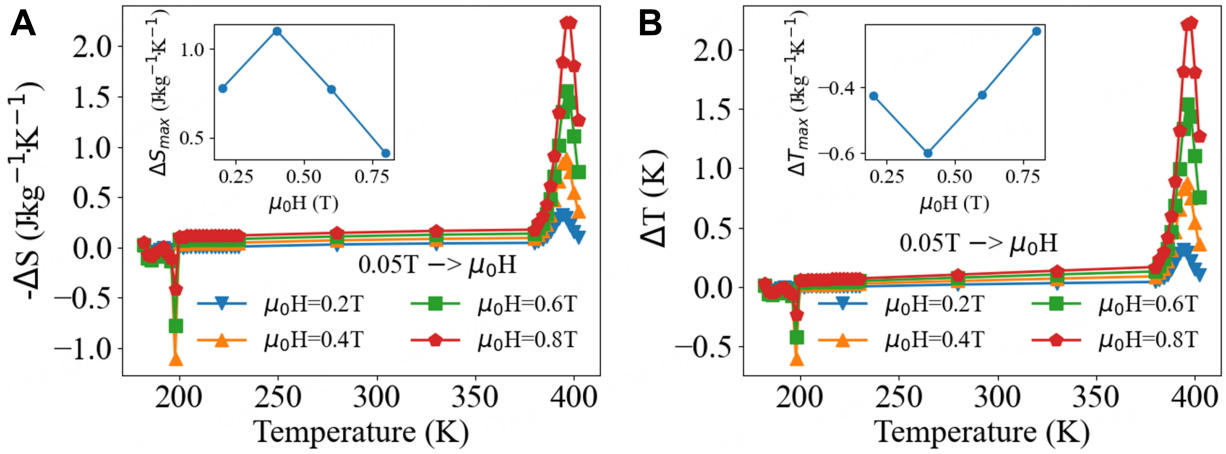

Figure 4. (A) Isothermal entropy changes of the inverse and conventional magnetocaloric effects. The inset is the maximum entropy change versus $\mu_0 H$ at 196 K; (B) Adiabatic temperature changes of the inverse and conventional magnetocaloric effect. The inset shows that the temperature change versus $\mu_0 H$ at 196 K.

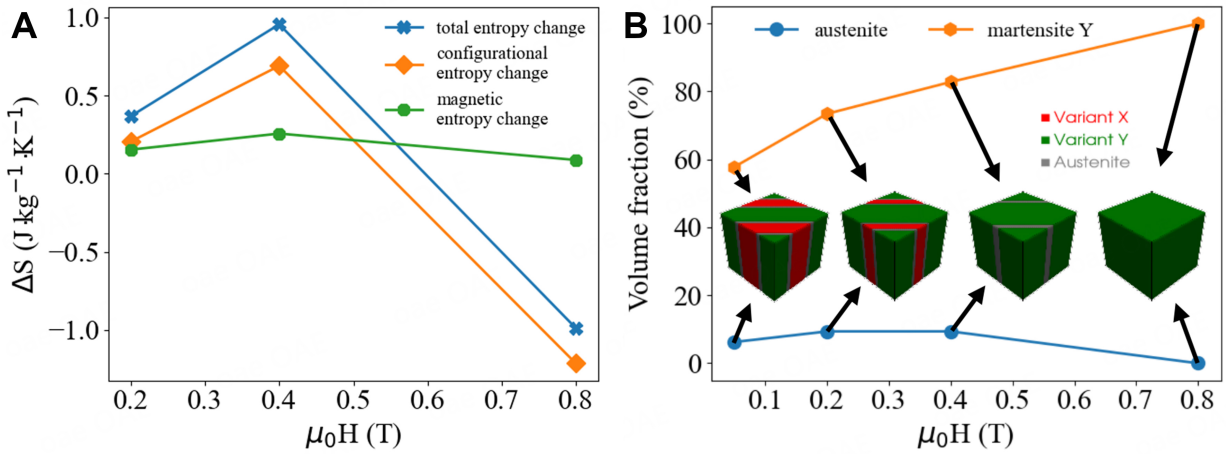

Figure 5. (A) Entropy contributions from different energy terms at 196 K as functions of magnetic fields; (B) Volume fractions of austenite and that of the martensite variant Y at 196 K as functions of magnetic fields along axis Y.

distinct magnetization regimes and clarified the microscopic origin of the inverse-to-conventional magnetocaloric crossover. In the phase-field model, the total free energy is decomposed into magnetic and structural contributions [see Eq. (1)]. Entropy is derived from the thermodynamic relation $S = -\left(\frac{\partial E}{\partial T}\right)_{H,p}$. The magnetic entropy is obtained from the purely magnetic energy terms, while the structural entropy is calculated from all remaining contributions. In the presence of low fields ($\mu_0 < 0.4$ T), structural entropy change is observed to dominate and exhibit a strongly positive trend. This phenomenon arises from the field-driven reorientation of the martensite variants Y-to-X and the coupled motion of twin boundaries. The variation of the volume fraction of martensite variants Y with the magnetic fields is demonstrated in Figure 5B. The magnetic entropy change is observed to be considerably less pronounced, resulting in a positive total entropy change, which is indicative of the inverse MCE. When $\mu_0 = 0.4$ T, it has been demonstrated that all variants Y are subject to full reorientation, thereby forming a monovariant state. This transition corresponds to the maximum positive structural entropy change. In the presence of a magnetic field exceeding 0.4 T, no additional structural rearrangements occur, and magnetization progresses exclusively through spin polarization. Conversely, structural entropy undergoes a precipitous decline, attaining strongly negative values, while magnetic entropy persists in a state of weakly negative variation. The total entropy change becomes negative, corresponding to the conventional MCE. The sign of entropy change reversal at 0.4 T corresponds to the critical field for complete variant reorientation and the peak cross coupling, thereby confirming the strong magnetostructural coupling that governs the magnetocaloric response.

The phenomenon is further substantiated by the temperature-dependent magnetization. In the range of magnetic fields below 0.4 T, $(\partial M/\partial T) > 0$ because the phenomenon of thermal activation becomes evident, facilitating twin boundary motion and variants reorientation. It has been established that the presence of a magnetic field with a magnitude greater than 0.4 T results in a negative outcome, i.e. $(\partial M/\partial T) < 0$. According to the Eq. (20) the positive $(\partial M/\partial T)$ below the field of 0.4T results in a positive entropy change, which is consistent with the inverse MCE at low fields. The negative slope above the field of 0.4T (and in the high-field single-domain state) yields a negative entropy change, consistent with the conventional MCE. This direct correlation confirms that the anomalous magnetocaloric response in Ni_2MnGa arises from the strong interplay among magnetic, structural, and configurational degrees of freedom. In this system, low-field behavior is controlled by the reorientation of martensite variants, and high-field behavior is governed by spin polarization.

This discovery has an applicable implication: maximum inverse MCE is achieved at the remarkably low field $\mu_0 H_C = 0.4$ T, which is substantially lower than the field required for conventional magnetocaloric materials. By adjusting the composition to position the operating temperature near T_M, the required critical field can be further reduced. This offers a new pathway for designing efficient low-field magnetic refrigeration devices.

Multicaloric effect and synergistic regulation by combined magnetic and pressure fields

In accordance with thermodynamic principles concerning the multicaloric effect, the aggregate isothermal entropy change caused by magnetic field and hydrostatic pressure can be expressed as the Eq. (22). As indicated in the relevant literature, cross-susceptibility under external magnetic and hydrostatic pressure fields, referred to as χ_{12}, is defined as follows:

$$\chi_{12} = -\left(\frac{\partial M}{\partial p}\right) = \left(\frac{\partial V}{\partial (\mu_0 H)}\right) = \left(\frac{\partial^2 E}{\partial p \partial (\mu_0 H)}\right) \tag{23}$$

In the present work, this coefficient is calculated from the mixed second-order derivative of the total free energy. The first two terms in Eq. (22) represent the individual magnetocaloric and barocaloric responses that were measured in the absence of a secondary field. The third term represents the cross-susceptibility contribution, which assumes significance when χ_{12} is temperature-dependent. The non-vanishing cross term is indicative of a genuine multicaloric response that cannot be decomposed into two independent mono-caloric effects.

A series of simulations were conducted in which hydrostatic pressure ranging from 0 to 1 GPa was applied concurrently with a magnetic field ranging from 0.05 to 0.8 T. As illustrated in Figures 6A and B, the isothermal entropy change ΔS and adiabatic temperature change ΔT of the multicaloric effect are shown respectively. In contrast to the non-monotonic evolution of the MCE, the multicaloric entropy and temperature changes vary monotonically with field strength. This phenomenon can be attributed to the suppression of magnetically induced reorientation of martensitic variants by hydrostatic pressure, thereby eliminating the structural-entropy-driven non-monotonicity of the MCE. The mechanical constraint has been demonstrated to enhance the effective magnetoelastic coupling, thereby increasing the system's sensitivity to magnetic fields. This phenomenon is evident in the steeper slope of the M-H curves observed under pressure.

A quantitative analysis reveals that the maximum entropy change of the BCE under the condition of p = 0 → 1 GPa is ΔS_{BCE} = -4.01 J·kg^{-1}·K^{-1}. It has been demonstrated that the maximum entropy change of the MCE, when considered under the parameter range of $\mu_0 H$ = 0.05 → 0.8 T, is ΔS_{MCE} = +0.40 J·kg^{-1}·K^{-1}. The sum of the entropy changes of the two individual mono-caloric effects is $\Delta S_{mono} = \Delta S_{BCE} + \Delta S_{MCE}$ = -3.61 J·kg^{-1}·K^{-1}. By contrast, under the condition of combined p = 0 → 1 GPa and $\mu_0 H$ = 0.05 → 0.8 T, the multicaloric entropy

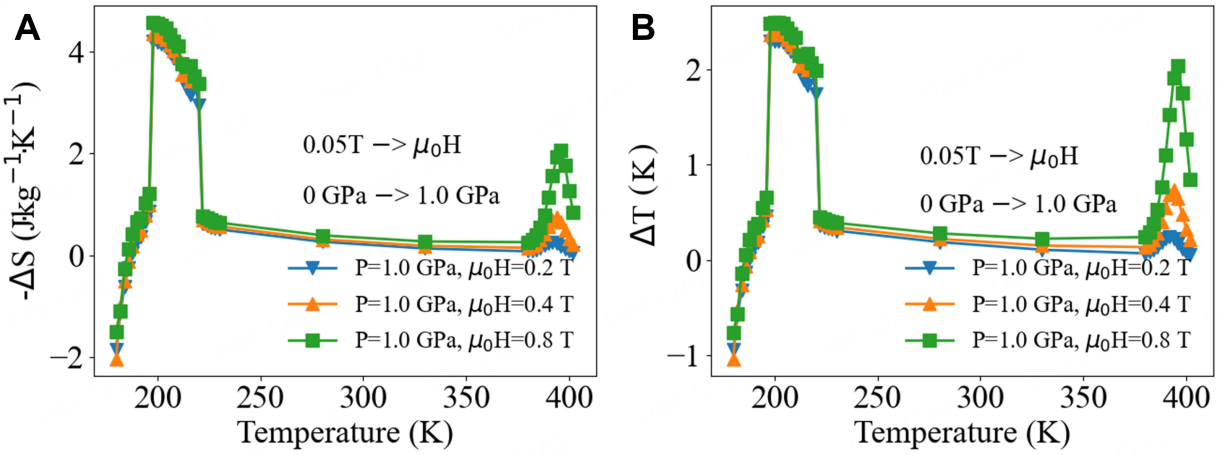

Figure 6. (A) Isothermal entropy changes and (B) adiabatic temperature changes of the multicaloric effect under different hydrostatic pressures and magnetic fields.

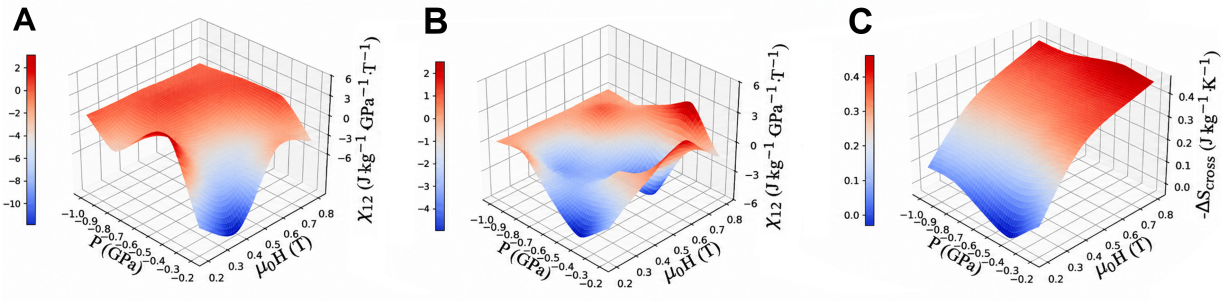

Figure 7. The cross-susceptibility χ_{12} and isothermal entropy change ΔS in Ni_2MnGa: (A) χ_{12} at 196 K and (B) χ_{12} at 198 K; (C) the correlated isothermal entropy change ΔS as a function of magnetic field and hydrostatic pressure.

change reaches ΔS_{multi} = -4.56 J·kg^{-1}·K^{-1}. It has been determined that the absolute value of ΔS_{multi} is greater than that of ΔS_{mono}. According to Eq. (22), the entropy change associated with the cross-susceptibility term is negative, indicating that pressure suppresses the motion of field-induced variants. The cross-susceptibility at 196 K and at 198 K was computed using Eq. (22). The results of this computation are shown in Figure 7A and B. As illustrated in Figure 7B, the minimum of χ_{12} observed at μ_0H = 0.3 ~ 0.4 T corresponds to the completion of martensite variants reorientation(martensite variants Y to X). The other minimum of χ_{12}, observed at higher magnetic fields, can be attributed to the nonlinear effect as magnetization approaches saturation. Then the entropy changes associated with the cross-susceptibility at 198 K were computed using Eq. (23). As demonstrated in Figure 7C, the entropy changes under the aforementioned conditions is negative. This finding serves to substantiate the hypothesis that Ni_2MnGa manifests a synergistic enhancement of the multicaloric effect.

CONCLUSIONS

In summary, the present study elucidates the cooperative regulation of the martensitic transformation and caloric responses in Ni_2MnGa by hydrostatic pressure and magnetic fields. Uniaxial pressure drives twin boundary migration to achieve a mono-variant state, enabling large reversible actuation . Concurrently, hydrostatic pressure simultaneously suppresses magnetically induced reorientation - tuning magnetic hysteresis - and raises the transformation temperature by ~24 K/GPa, thereby boosting the BCE. The magnetocaloric response displays a field-driven transition: at fields below 0.4 T, variant reorientation generates a positive structural entropy change (inverse MCE); above this critical field, spin polarization

dominates, yielding a negative entropy change (conventional MCE). This reversal is directly tied to the completion of structural reorientation and strong magnetostructural coupling. It has been demonstrated that the non-monotonicity of the MCE is eliminated under the combined pressure and magnetic field. Consequently, the multicaloric response becomes monotonic and synergistically enhanced, with an entropy change exceeding the sum of individual contributions due to negative magnetoelastic cross-coupling. These results establish a thermodynamic pathway for engineering high-performance multicaloric materials through controlled external-field interactions.

DECLARATIONS

Authors' contributions

Made substantial contributions to conception and design of the study and performed data analysis and interpretation: Dong, M.; Shi, X.; Ma, X.

Performed data acquisition, as well as provided administrative, technical, and material support: Liu, J.; Wang, H.; Wang, Z.; Liu, Z.; Chen, J.; Huang, H.

Availability of data and materials

The data that support the findings of this study are available from the corresponding author upon reasonable request.

AI and AI-assisted tools statement

Not applicable.

Financial support and sponsorship

This work was supported by the National Key Research and Development Program of China (No. 2017YFB0702702), the Fundamental Research Funds for the Central Universities (No. FRF-BRB-25-006, No. FRF-TP-24-041A),2023 Fund for Fostering Young Scholars of the School of Mathematics and Physics, USTB (FRF-BR-23-01B), the National Natural Science Foundation of China (No. 22235002), the Open Project Fund from Guangdong Provincial Key Laboratory of Materials and Technology for Energy Conversion, Guangdong Technion-Israel Institute of Technology (No. MATEC2024KF008).

Conflicts of interest

Chen, J. is an Executive Editor of the journal *Microstructures*. Huang, H. is an Associate Editor of the journal *Microstructures*. Chen, J. and Huang, H. were not involved in any steps of editorial processing, notably including reviewers' selection, manuscript handling or decision making. The other authors declare that there are no conflicts of interest.

Ethical approval and consent to participate

Not applicable.

Consent for publication

Not applicable.

REFERENCES

1. Stern-taulats, E.; Castán, T.; Mañosa, L.; Planes, A.; Mathur, N. D.; Moya, X. Multicaloric materials and effects. *MRS. Bull.* **2018**, *43*, 295-9. DOI
2. Pal, D. A short review of magnetocaloric effect in Ni-Mn-Ga heusler alloy system. *Int. J. Sci. Res. Phys. Appl. Sci.* **2023**, *11*, 13-20. https://inis.iaea.org/records/0pmfh-5qh81. (accessed 2026-06-30).
3. Kitanovski, A. Energy applications of magnetocaloric materials. *Adv. Energy. Mater.* **2020**, *10*, 1903741. DOI
4. Yu, C.; Chen, T.; Yin, H.; Kang, G.; Fang, D. Modeling the anisotropic elastocaloric effect of textured NiMnGa ferromagnetic shape memory alloys. *Int. J. Solids. Struct.* **2020**, *191-2*, 509-28. DOI

5. Cirillo, L.; Greco, A.; Masselli, C. Cooling through barocaloric effect: a review of the state of the art up to 2022. *Therm. Sci. Eng. Prog.* **2022**, *33*, 101380. DOI
6. Sun, Y.; An, S.; Gao, Y.; et al. Materials with the barocaloric effect for solid-state refrigeration. *J. Mater. Chem. A.* **2025**, *13*, 6152-75. DOI
7. Mañosa, L.; Planes, A. Solid-state cooling by stress: a perspective. *Appl. Phys. Lett.* **2020**, *116*, 050501. DOI
8. Boldrin, D. Fantastic barocalorics and where to find them. *Appl. Phys. Lett.* **2021**, *118*, 170502. DOI
9. Greco, A.; Aprea, C.; Maiorino, A.; Masselli, C. A review of the state of the art of solid-state caloric cooling processes at room-temperature before 2019. *Int. J. Refrig.* **2019**, *106*, 66-88. DOI
10. Stern-taulats, E.; Planes, A.; Lloveras, P.; et al. Tailoring barocaloric and magnetocaloric properties in low-hysteresis magnetic shape memory alloys. *Acta. Materialia.* **2015**, *96*, 324-32. DOI
11. Gorev, M.; Bogdanov, E.; Flerov, I. Conventional and inverse barocaloric effects around triple points in ferroelastics $(NH_4)_3$ $NbOF_6$ and $(NH_4)_3$ $TiOF_5$. *Scr. Mater.* **2017**, *139*, 53-7. DOI
12. Mikhaleva, E. A.; Flerov, I. N.; Gorev, M. V.; et al. Caloric characteristics of PbTiO3 in the temperature range of the ferroelectric phase transition. *Phys. Solid. State.* **2012**, *54*, 1832-40. DOI
13. Lloveras, P.; Aznar, A.; Barrio, M.; et al. Colossal barocaloric effects near room temperature in plastic crystals of neopentylglycol. *Nat. Commun.* **2019**, *10*, 1803. DOI PubMed PMC
14. Sagotra, A. K.; Chu, D.; Cazorla, C. Room-temperature mechanocaloric effects in lithium-based superionic materials. *Nat. Commun.* **2018**, *9*, 3337. DOI PubMed PMC
15. Carvalho, A.; Imamura, W.; Usuda, E.; Bom, N. Giant room-temperature barocaloric effects in PDMS rubber at low pressures. *Eur. Polym. J.* **2018**, *99*, 212-21. DOI
16. Usuda, E.; Bom, N.; Carvalho, A. Large barocaloric effects at low pressures in natural rubber. *Eur. Polym. J.* **2017**, *92*, 287-93. DOI
17. Hu, F.; Wei, S.; Cao, Y.; et al. Magnetocaloric and barocaloric effects associated with two successive magnetostructural transformations in $Ni_{55.5}Mn_{17.8}Ga_{26.7}$ alloy. *J. Alloys. Compd.* **2020**, *818*, 153356. DOI
18. Pataky, G. J.; Ertekin, E.; Sehitoglu, H. Elastocaloric cooling potential of NiTi, Ni_2FeGa, and CoNiAl. *Acta. Materialia.* **2015**, *96*, 420-7. DOI
19. Eerenstein, W.; Mathur, N. D.; Scott, J. F. Multiferroic and magnetoelectric materials. *Nature* **2006**, *442*, 759-65. DOI PubMed
20. Cong, D.; Xiong, W.; Planes, A.; et al. Colossal elastocaloric effect in ferroelastic Ni-Mn-Ti alloys. *Phys. Rev. Lett.* **2019**, *122*, 255703. DOI PubMed
21. Imran, M.; Zhang, X. Elastocaloric effects in polycrystalline Ni-Fe-Ga foams with hierarchical pore architecture. *Phys. Rev. Materials.* **2020**, *4*, 065403. DOI
22. Mañosa, L.; González-Alonso, D.; Planes, A.; et al. Giant solid-state barocaloric effect in the Ni-Mn-In magnetic shape-memory alloy. *Nat. Mater.* **2010**, *9*, 478-81. DOI PubMed
23. Liu, K.; Zeng, H.; Qi, J.; et al. Microstructure and giant baro-caloric effect induced by low pressure in Heusler $Co_{51}Fe_1V_{33}Ga_{15}$ alloy undergoing martensitic transformation. *J. Mater. Sci. Technol.* **2021**, *73*, 76-82. DOI
24. Nguyen, H. Y.; Kieu, X. H.; Nguyen, H. N.; et al. Structure and magnetic properties of Ni-Mn-Ga shape memory alloys. *Adv. Nat. Sci.:. Nanosci. Nanotechnol.* **2022**, *13*, 015014. DOI
25. Tao, J.; Yang, X.; Liu, X.; Wu, J.; Wang, Y. Effects of hydrostatic pressure on martensitic transition, ductility, and magnetocrystalline anisotropy of Ni_2MnGa. *J. Appl. Phys.* **2025**, *137*, 245902. DOI
26. Wu, P.; Ma, X.; Zhang, J.; Chen, L. Phase-field simulations of magnetic field-induced strain in Ni_2MnGa ferromagnetic shape memory alloy. *Philos. Mag.* **2011**, *91*, 2102-16. DOI
27. Ohmer, D.; Yi, M.; Gutfleisch, O.; Xu, B. Phase-field modelling of paramagnetic austenite-ferromagnetic martensite transformation coupled with mechanics and micromagnetics. *Int. J. Solids. Struct.* **2022**, *238*, 111365. DOI
28. Jin, Y. M. Domain microstructure evolution in magnetic shape memory alloys: phase-field model and simulation. *Acta. Mater.* **2009**, *57*, 2488-95. DOI
29. Huang, H.; Ma, X.; Wang, J.; Liu, Z.; He, W.; Chen, L. A phase-field model of phase transitions and domain structures of NiCoMnIn metamagnetic alloys. *Acta. Mater.* **2015**, *83*, 333-40. DOI
30. Zayak, A.; Buchelnikov, V.; Entel, P. A Ginzburg-Landau theory for Ni-Mn-Ga. *Phase. Transit.* **2002**, *75*, 243-56. DOI
31. Yeddu, H. K.; Malik, A.; Ågren, J.; Amberg, G.; Borgenstam, A. Three-dimensional phase-field modeling of martensitic microstructure evolution in steels. *Acta. Mater.* **2012**, *60*, 1538-47. DOI
32. Cui, S.; Wan, J.; Zuo, X.; Chen, N.; Zhang, J.; Rong, Y. Three-dimensional, non-isothermal phase-field modeling of thermally and stress-induced martensitic transformations in shape memory alloys. *Int. J. Solids. Struct.* **2017**, *109*, 1-11. DOI

33. Vasil'ev, A.; Bozhko, A.; Khovailo, V.; et al. Structural and magnetic phase transitions in shape memory alloys $Ni_{2+x}Mn_{1-x}Ga$. *J. Magn. Magn. Mater.* **1999**, *196-197*, 837-9. DOI
34. Wang, X.; García-cervera, C. J.; Weinan, E. A gauss-seidel projection method for micromagnetics simulations. *J. Comput. Phys.* **2001**, *171*, 357-72. DOI
35. Cejpek, P.; Proschek, P.; Straka, L.; Heczko, O. Dependence of martensite transformation temperature on magnetic field in Ni_2MnGa and $Ni_2MnGa_{0.95}In_{0.05}$ single crystals. *J. Alloys. Compd.* **2022**, *908*, 164514. DOI
36. Vasil'ev, A. N.; Buchel'nikov, V. D.; Takagi, T.; Khovailo, V. V.; Estrin, E. I. Shape memory ferromagnets. *Phys. -Usp.* **2003**, *46*, 559-88. DOI
37. Maeda, H.; Fukuda, T.; Kakeshita, T. Effect of hydrostatic pressure on martensitic transformation in a ferromagnetic shape memory alloy Ni_2MnGa. *J. Alloys. Compd.* **2011**, *509*, 7840-3. DOI
38. He, X. J.; Xu, K.; Wei, S. X.; Zhang, Y. L.; Li, Z.; Jing, C. Barocaloric effect associated with magneto-structural transformation studied by an effectively indirect method for the $Ni_{58.3}Mn_{17.1}Ga_{24.6}$ Heusler alloy. *J. Mater. Sci.* **2017**, *52*, 2915-23. DOI
39. Radelytskyi, I.; Pękała, M.; Szymczak, R.; et al. Magnetocaloric effect in Ni_2MnGa single crystal in the vicinity of the martensitic phase transition. *J. Magn. Magn. Mater.* **2017**, *430*, 16-21. DOI